1. Results from prior NSF support

Three of the four PI's, Alarcon, Baeßler and Počanić, have current and/or prior NSF support; the grant specifics are listed under "Current and Pending Support." Prior and current NSF support for all three PI's has been instrumental in enabling the preparation of this proposal.

Alarcon's NSF grants PHY-0652394 and -0969654 have supported three graduate students, one postdoctoral research associate, and three undergraduate students. Result highlights include the completion of the RDK-II experiment: a precise measurement of the neutron radiative decay rate at NIST, the mounting of the OLYMPUS experiment to measure the effect of multiple photon exchange in lepton scattering at DESY, the commissioning of the NPDGamma experiment to study the strength of the hadronic weak interaction at the SNS, and the publication of nucleon form factors results from the BLAST experiment at MIT-Bates.

Baessler is funded since 2009 by NSF grant PHY-0855610, which has supported several undergraduate students, one graduate student, and a postdoc. Result highlights include a key conceptual change of the common Nab and abBA spectrometer (discussed below), and the selection of the surface coating with a suppressed patch effect for the Nab electrode system. The patch effect is the limiting factor in the electrostatic potential homogeneity for the electrode. One M.Sc. has resulted from this work so far.

Počanić's NSF support, going back over 20 years, has enabled his group's leading role in several experimental programs, most recently PIBETA and PEN at PSI, and Nab at SNS, and has resulted in over 100 publications in refereed journals. Most significant recent results are the new precise values for rare pion and muon decay branching ratios. The >20 graduate students and postdocs trained in this program are listed in Počanić's bigraphical sketch, attached below.

2. Project description

Instrument Location: Oak Ridge National Laboratory, Oak Ridge, Tennessee.
Instrument Code: MRI-61, Sub-atomic particle detector/array.

The proposed research instrument will be used in a program of precise experimental study of the neutron beta decay. This research falls within the broader field of study of the basic properties and symmetries of the electroweak interaction at low energies. Although successful without parallel, the present standard model based on the $SU(3)_c \otimes SU(2)_L \otimes U(1)_Y$ gauge symmetries, is known to be incomplete, i.e., additional particles and phenomena must exist. Questions regarding possible extensions of the SM are being simultaneously addressed at the high energy frontier, using particle colliders, and at the precision frontier at low and intermediate energies. The program of study proposed here belongs in the latter category, and strives to illuminate the questions pertaining to the number of quark generations (through exploring quark-lepton universality via the Cabibbo–Kobayashi–Maskawa/CKM matrix), non-SM forms of weak interaction (i.e., scalar, pseudoscalar and tensor), couplings to right-handed intermediate bosons and fermions, as well as trace evidence of supersymmetry.

The proposed program of study will be carried out at the Fundamental Neutron Physics Beamline of the Spallation Neutron Source, in Oak Ridge, Tennessee. The Nab experiment will run first and measure the decay parameters in unpolarized neutron decay. The abBA will follow, focusing on the parameters om polarized neutron decay. The two experiments will share the same basic apparatus, at the core of which lies the magneto-electrostatic spectrometer, the instrument whose funding is requested here. Both experiments have been approved by the FnPB Proposal Research and Advisory Committee (PRAC).

2.1. Physics motivation

Neutron β decay, $n \to pe\bar{\nu}_e$, is one of the basic processes in nuclear physics. Its experimental study provides the most sensitive means to evaluate the ratio of axial-vector to vector coupling constants $\lambda = G_A/G_V$. The precise value of λ is important in many applications of the theory of weak interactions, especially in astrophysics; e.g., a star's neutrino production is proportional to λ^2. More precise measurements of neutron β-decay parameters are also important in the search for new physics. Measurement of the neutron decay rate Γ, or lifetime $\tau_n = 1/\Gamma$, allows a determination of V_{ud}, the u-d Cabibbo-Kobayashi-Maskawa (CKM) matrix element, independent of nuclear models, because Γ is proportional to $|V_{ud}|^2$, as seen in the leading order expression:

$$\Gamma = \frac{1}{\tau_n} = \frac{f^R m_e^5 c^4}{2\pi^3 \hbar^7} \left(|G_V|^2 + 3|G_A|^2\right) \propto |G_V|^2 \left(1 + 3|\lambda|^2\right) = |V_{ud}|^2 \, |g_V|^2 \, G_F^2 (1 + 3|\lambda|^2) \,, \tag{1}$$

where $f^R = 1.71482(15)$ is a phase space factor, m_e is the electron mass, $g_{V,A}$ the vector and axial-vector weak nucleon form factors at zero momentum transfer, respectively, and G_F is the fundamental Fermi weak coupling constant. While the conservation of vector current (CVC) fixes g_V at unity, two unknowns, V_{ud} and λ, remain as variables in the above expression for Γ. Hence, an independent measurement of λ is necessary in order to determine V_{ud} from the neutron lifetime. Several neutron decay parameters can be used to measure λ; they are discussed below. Precise knowledge of V_{ud} helps greatly in establishing the extent to which the three-generation CKM matrix is unitary. CKM unitarity, in turn, provides an independent cross-check of the presence of certain processes and particles not included in the Standard Model (SM) of elementary particles and interactions, i.e., an independent constraint on new physics.

Currently, the most accurate value of the CKM matrix element V_{ud} is obtained from measurements of $0^+ \to 0^+$ nuclear β-decays, the so-called superallowed Fermi transitions [1]. However, the procedure of the extraction of V_{ud} involves calculations of radiative and nuclear structure corrections for the Fermi transition in nuclei. Despite the fact that these calculations have been done with high precision (see [7] and references therein), it is impossible to verify the values of these nuclear corrections from independent experiments, and, as discussed below, questions concerning these corrections have been raised.

A problem with CKM matrix unitarity at the $2-3\sigma$ level persisted for over two decades. For example, the 2002 Review of Particle Properties [2] reported values of CKM matrix elements that yield for the first row

$$\Delta \equiv 1 - |V_{ud}|^2 - |V_{us}|^2 - |V_{ub}|^2 = (32 \pm 14) \times 10^{-4}\,. \tag{2}$$

The situation changed drastically in 2003 and 2004 when a series of experiments at Brookhaven, Fermilab and CERN reported revised values of K_{l3} decay branching ratios, leading to an upward adjustment, by about 2.5σ, of the CKM matrix element V_{us} [3, 4, 5]. Skipping the details of this revolutionary development, we note that a revised CKM unitarity check yields [6, 7, 1] $\Delta = (1 \pm 10) \times 10^{-4}$. Thus, at least for a few years, the question of the CKM matrix unitarity appeared to be closed. However, several authors have recently questioned the Hardy and Towner analysis of superallowed Fermi $0^+ \to 0^+$ transitions [7], finding isospin-related corrections to be larger, thus leading to a smaller value for V_{ud}, and to possible CKM unitarity violation [8, 9, 10, 11, 12]. This matter clearly remains to be definitively resolved.

Given the intrinsic theoretical complexity of nuclear beta decays, it is highly desirable to have an independent check of the superallowed Fermi nuclear beta decay result; neutron beta decay provides an excellent opportunity for that. Regrettably, a disturbing inconsistency persists between the best results on neutron decay and those on nuclear Fermi decays, as well as within the body of the neutron decay data.

Additionally, by its nature, neutron decay offers redundant consistency checks whose failure can be an indication of new physics.

We begin to discuss the last two points by briefly examining the neutron decay dynamics. Neglecting nucleon recoil, as well as radiative and loop corrections, the triple differential neutron decay rate is determined by the decay parameters a, b, A, B, etc., as shown:

$$\frac{dw}{dE_e d\Omega_e d\Omega_\nu} \propto p_e E_e (E_0 - E_e)^2 \left[1 + a\frac{\vec{p}_e \cdot \vec{p}_\nu}{E_e E_\nu} + b\frac{m_e}{E_e} + \langle \vec{\sigma}_n \rangle \cdot \left(A\frac{\vec{p}_e}{E_e} + B\frac{\vec{p}_\nu}{E_\nu} + \ldots \right) \right], \tag{3}$$

where $p_{e(\nu)}$ and $E_{e(\nu)}$ are the electron (neutrino) momenta and energies, respectively, E_0 is the electron energy spectrum endpoint, and $\vec{\sigma}_n$ is the neutron spin. The "lower-case" parameters: a, the electron–neutrino correlation, and b, the Fierz interference term, are measurable in decays of unpolarized neutrons, while the "uppercase" parameters, A and B, require polarized neutrons. Within the Standard Model, all except b depend on the ratio $\lambda = g_A/g_V$, in the following way (given here at the tree level, with λ real):

$$a = \frac{1 - |\lambda|^2}{1 + 3|\lambda|^2}\,, \qquad A = -2\frac{|\lambda|^2 + \lambda}{1 + 3|\lambda|^2}\,, \qquad B = 2\frac{|\lambda|^2 - \lambda}{1 + 3|\lambda|^2}\,. \tag{4}$$

Given that $\lambda \simeq -1.27$, parameters A and a are similarly sensitive to λ, while B is relatively insensitive:

$$\frac{\partial a}{\partial \lambda} \simeq 0.30\,, \qquad \frac{\partial A}{\partial \lambda} \simeq 0.37\,, \qquad \frac{\partial B}{\partial \lambda} \simeq 0.076\,. \tag{5}$$

Experimental status of the above parameters is summarized in the Particle Data Group's review in Ref. [1]. For some time, the best precision by far in extracting λ has been achieved through measurement of A, the

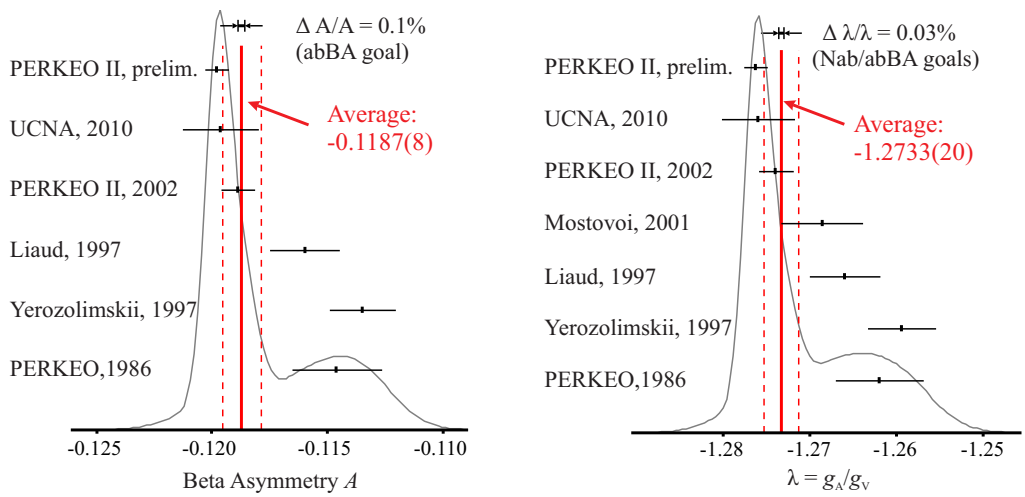

Figure 1: Updated compilation of the most precise measurements of the neutron beta asymmetry A (left panel) and λ (right panel). Data are from the UCNA experiment [13], PERKEO II (preliminary) [14], PERKEO [15], Liaud et al. [16], Yerozolimsky et al. [17], Bopp et al. [18] and Mostovoi et al. [19]. The average values, $A = -0.1187(8)$ and $\lambda = -1.2733(20)$, respectively, include scale factors greater than 2, reflecting low statistical probabilities associated with the high χ^2 values of the fits. At the top, the estimated sensitivities of Nab and abBA are shown.

correlation between the electron momentum and neutron spin. However, the experimental status of A and λ is far from satisfactory, as seen below.

Two beta asymmetry experiments finished their analysis recently, since the most recent PDG compilation. The UCNA collaboration published the value $A = -0.11966(89)(^{+123}_{-140})$ [13]. The result of the last PERKEO II run, $A = -0.1198(5)$, will be published soon [14]. If we include these new results along with those from previous experiments in a new average, in the same way as done by PDG [1], we obtain $A = -0.1187(8)$ with $\chi^2 = 28$ for 5 degrees of freedom, which is even less satisfactory than the previously reported PDG result (see Fig. 1). This disagreement carries over directly to the value of λ and, hence, to V_{ud}. One of the principal goals of the proposed Nab and abBA experiments are independent determination of λ from a, the neutrino electron correlation coefficient, and A, the beta asymmetry, respectively. We show in Fig. 1 the impact of the measurement of A with $\Delta A/A = 10^{-3}$, which is achievable with abBA. The impact of such a measurement on λ is identical to that of a measurement of a with $\Delta a/a = 10^{-3}$ with Nab, and is shown in the right panel of the same figure. The Nab measurement of a will have entirely different systematic uncertainties from the best measurements of the beta asymmetry A, and may even be more precise.

We also note that recent studies of $T = \frac{1}{2}$ nuclear mirror transitions [20] have reached the precision of V_{ud} determination achieved thus far with neutron beta decays, i.e., through measurements of A, the beta asymmetry, and τ_n, neutron lifetime, as discussed above.

Just as interesting as the determination of $\lambda = G_A/G_V$ are the limits on non-SM interactions that can be extracted from studies of neutron beta decay. Multiple measurements of neutron decay correlation coefficients and the neutron lifetime on the one hand, and the well known lifetime of superallowed decays have been used to search for physics beyond the standard model. In the low energy limit, semileptonic decays can be universally described by a point-like interaction between currents of different type (vector, axial-vector, scalar, and tensor), and of different handedness.

$$H_{\rm if} = \frac{2G_{\rm F}V_{\rm ud}}{\sqrt{2}} \sum_{j\in\{\rm V,A,S,T\}} L_j \langle p|\,\Gamma_j\,|n\rangle \left\langle e^-\middle|\,\Gamma_j \frac{1-\gamma_5}{2}\,|\nu_e\right\rangle + R_j \langle p|\,\Gamma_j\,|n\rangle \left\langle e^-\middle|\,\Gamma_j \frac{1+\gamma_5}{2}\,|\nu_e\right\rangle . \qquad (6)$$

The types of currents are defined by the operators $\Gamma_{\rm V} = \gamma_\mu$; $\Gamma_{\rm A} = i\gamma_\mu\gamma_5$; $\Gamma_{\rm S} = 1$; $\Gamma_{\rm T} = i\left[\gamma_\mu, \gamma_\nu\right]/(2\sqrt{2})$. The coupling constants leading to a left-handed neutrino and a right handed neutrino are denoted L_j and R_j, respectively. This parametrization was introduced by Glück et al. [21]; these coupling constants are linear

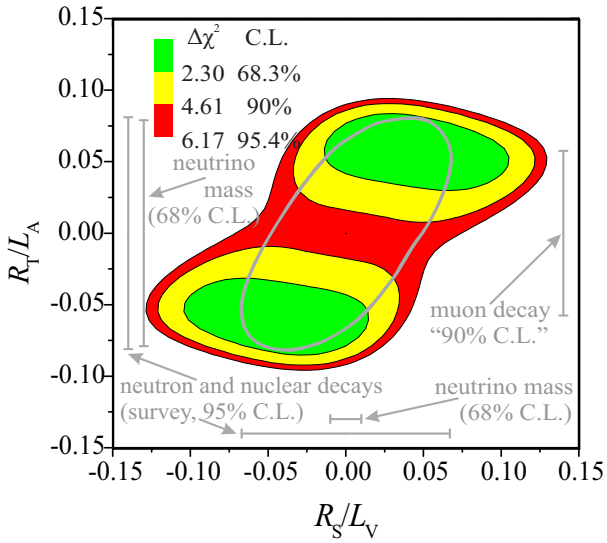

Figure 2: Present limits for right-handed scalar and tensor currents from neutron decay. The standard model prediction is at the origin of the plot. Analogous tensor limits extracted from muon decays are indicated as well—the scalar limits are larger than the scale of the plot (see text for details).

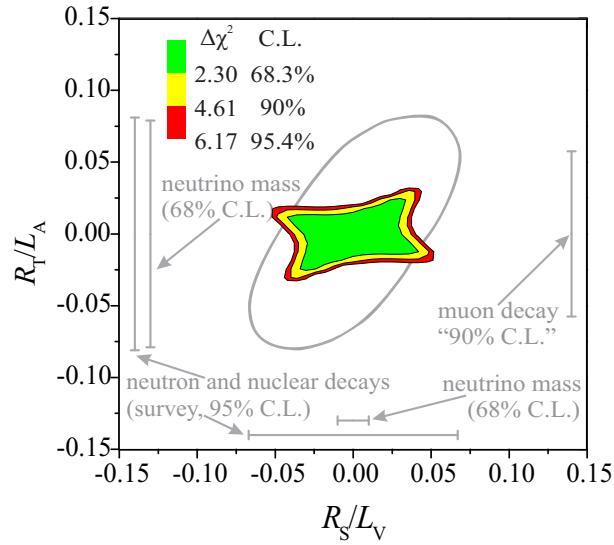

Figure 3: Future limits for right-handed scalar and tensor currents from neutron decay. The black lines are present 68.3% and 95.4% contours found in a recent survey of nuclear and neutron beta decays [27]. Analogous tensor limits extracted from muon decays (see text for details) are also indicated—the scalar limits are larger than the scale of the plot.

combinations of C_j and C'_j, the familiar couplings originally introduced in the 1950's [22, 23]:

$$C_j = \frac{G_{\rm F} V_{\rm ud}}{\sqrt{2}} \left(L_j + R_j\right), \; C'_j = \frac{G_{\rm F} V_{\rm ud}}{\sqrt{2}} \left(L_j - R_j\right) \;\text{ for } j = {\rm V, A, S, T}\,. \tag{7}$$

In the standard model, the only nonvanishing coupling constants are $L_{\rm V} = 1$ (CVC) and $L_{\rm A} = \lambda$. In more general models, other coupling constants appear and certain measurement observables are modified. Details are given in Refs. [21, 22, 23].

The most recent compilation of limits from neutron decay and their comparison to nuclear and other particle physics processes is published in Ref. [24]; two of the present co-PI's are coauthors. This work used the value $\tau_{\rm n} = 881.9(14)\,{\rm s}$ ([1] and [25]) for the neutron lifetime, $Ft = 3071.81\,{\rm s}$ from superallowed beta decays [7], the beta asymmetry $A = -0.1186(9)$, the neutrino asymmetry $B = 0.9807(30)$ [1], and the neutrino electron correlation coefficient $a = -0.1030(40)$ [1] as input parameters. Newer results shift the averages for neutron lifetime (Ref. [26], new average $\tau_{\rm n} = 881.8(13)\,{\rm s}$), and for the beta asymmetry (UCNA, Ref. [13], new average $A = -0.1187(8)$). The resulting changes are not substantial, either in the average value and its uncertainty, or in the statistical confidence. Below we update the analysis of Ref. [24] with the revised input values.

We first consider the sensitivity to right-handed scalar and tensor currents. Figure 2 shows the status using the above averages, while Fig. 3 shows the improvement arising from an additional Nab measurement with $\Delta a/a = 10^{-3}$ (reflecting the projected Nab uncertainty), and an additional beta asymmetry measurement (e.g., from abBA) with $\Delta A/A = 10^{-3}$. The black lines stem from a recent survey of the state of the art in nuclear and neutron beta decays [27]. The plot clearly demonstrates that the proposed measurements of a and A in neutron decay are competitive with, and complementary to, other methods. We note that the exclusion limits in Fig. 3 change shape substantially if we choose central values for our input parameter which are not consistent with the SM, reflecting the fact that the observables depend quadratically on the non-SM coupling constants. In this standard model extension, as well as in the SM itself, the Fierz interference term b has to be zero.

For completeness, we also consider the limits on non-(V−A) interaction couplings extracted from muon

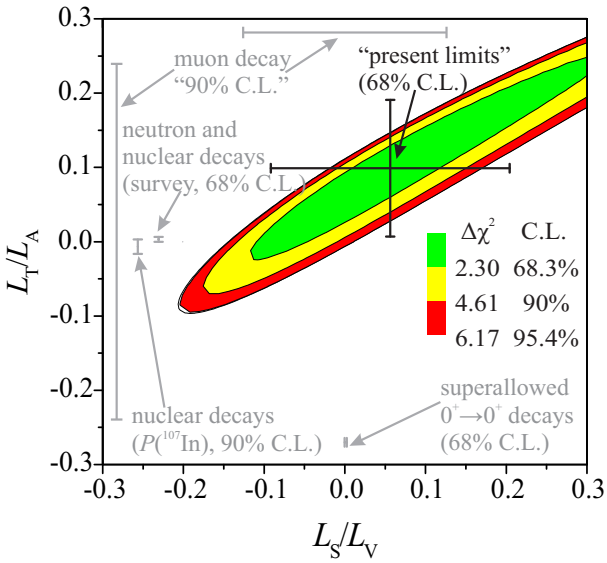

Figure 4: Present limits for left-handed scalar and tensor currents from neutron decay. The standard model prediction is at the origin of the plot. Analogous limits extracted from muon decays (see text for details) are also indicated.

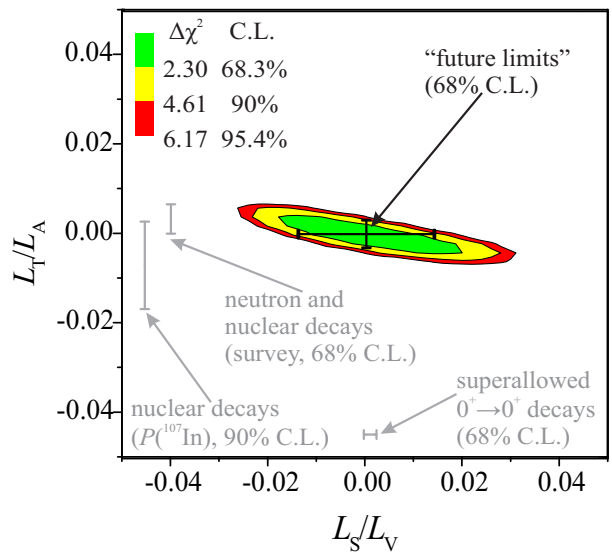

Figure 5: Future limits for left-handed scalar and tensor currents from neutron decay, assuming Nab measurements with $\Delta a/a = 10^{-3}$ for the neutrino correlation coefficient, and $b = 0 \pm 0.003$ for the Fierz term, and an abBA measurement with $\Delta A/A = 10^{-3}$.

decay measurements [28, 1]. These limits relate to operators that are different from the ones encountered in neutron beta decays. However, in certain supersymmetric extensions of the standard model, the muon and neutron decay derived limits become comparable [29, 30]. For this reason we have included the corresponding limits from muon decays in Figs. 2 – 5, as appropriate. Limits from neutrino mass measurements are discussed in [24].

We next turn to a model with left-handed scalar and tensor currents. In this model, a non-vanishing Fierz term b appears, and its measurement is a very sensitive way to constrain the size of the non-standard currents. Fig. 4 shows the current limits from neutron decay. Compared to the input data for Fig. 2, we leave out the nuclear and neutron lifetimes, since the Ft value used is obtained assuming a vanishing Fierz term (The Fierz term in superallowed decays, $b_{\rm F}$, is related, but not identical to the one in neutron decay due to the different matrix elements). Figure 5 demonstrates the impact of the projected Nab measurements of the neutrino–electron correlation coefficient a and the Fierz interference term b, and of the abBA measurement of the beta asymmetry A. For comparison, a recent combined analysis of neutron and nuclear physics data (see Ref. [27]) finds $L_{\rm S}/L_{\rm V} = 0.0013(13)$ and $L_{\rm T}/L_{\rm A} = 0.0036(33)$. New neutron data, in combination with the updated limit on $L_{\rm S}$ from the limits on $b_{\rm F}$ in superallowed beta decays [7], would improve the limit on $L_{\rm T}$ to $|L_{\rm T}| < 0.0016$. Supersymmetric contributions to the standard model can be discovered at this level of precision, as discussed in [29].

As a final note, we comment on comparisons with similar limits extracted from pion decays. The presence of a tensor interaction would manifest itself in both the Fierz interference term in beta decays (e.g., of the neutron), and in a non-zero value of the tensor form factor for the pion. The latter was hinted at for well over a decade, but was recently found to be constrained to $-5.2 \times 10^{-4} < F_T < 4.0 \times 10^{-4}$ with 90% confidence [31]. While values for b in neutron decay and for the pion F_T are not directly comparable, they could be of the same order [32]. Thus, finding a nonzero value for b in neutron decay at the level of $\mathcal{O}(10^{-3})$ would be extremely interesting. Similarly, the $\pi \to e\nu$ decay (π_{e2}) offers a very sensitive means to study non-(V−A) weak couplings, primarily through a pseudoscalar term in the amplitude. (Alternatively, π_{e2} decay provides the most sensitive test of lepton universality.) Thus, the measurements proposed here will complement the

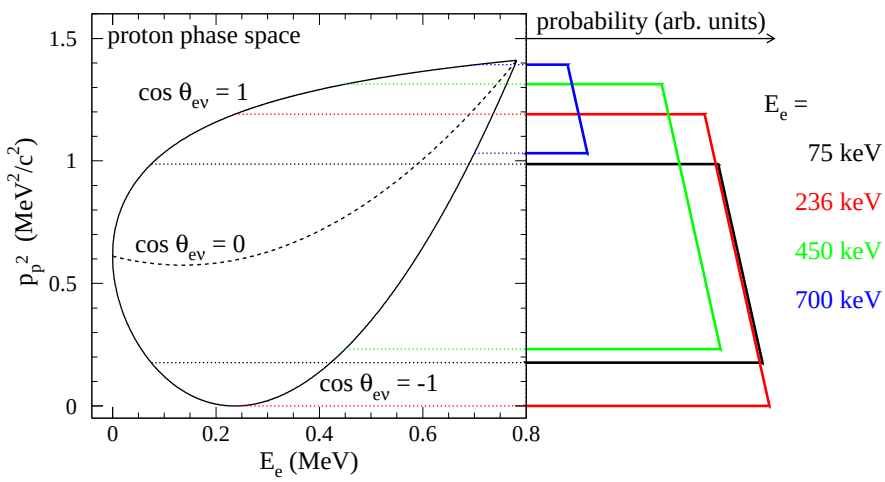

Figure 6: Decay phase space for electron (E_e) and proton energy ($\propto p_\mathrm{p}^2$), with curves of constant $\cos\theta_{e\nu}$ indicated. If the e–ν correlation $a = 0$, the probability distribution of p_p^2 for a given E_e would be uniform, i.e., a rectangular box spectrum. Expected probability distributions are projected to the right for $a = -0.103$, for four electron energies.

results of precision experiments in the pion sector, such as PIBETA [33], PEN [34], PiENu [35].

2.2. Design of the magneto-electrostatic spectrometer

The spectrometer design is driven to a large extent by the challenge of the measurement of a, the electron–neutrino correlation. Our method requires the detection of both the proton and electron in neutron decay, and the determination of their energies or momenta. This basic principle is illustrated in Fig. 6 which plots the available phase space in the p_p^2-E_e plane. The plot shows that a is determined by measuring the slope of the p_p^2 probability distribution for fixed E_e. While the Fierz interference term could in principle be determined from a precise measurement of the beta energy spectrum alone, coincident detection of the accompanying proton is essential in suppressing the singles background.

The basic idea of the proton time of flight (TOF) spectrometer was introduced in the Nab proposal [36] and subsequently published in Ref. [37]. Neutrons decay in a magnetic field that guides the electrons and protons to large-area segmented Si detectors. After a rapid field expansion region, the magnetic field is weak for most of the flight path, and the proton and electron momenta are nearly parallel to the field. Hence, the measured proton time of flight yields the proton energy. The pulse height in the Si detectors gives the electron energy. Since the proton recoil kinetic energy is negligible, the angle between the electron and neutrino is inferred from the proton and electron energies (or momenta), as shown below.

We determine the neutrino electron correlation coefficient for each electron energy E_e with a fit to the measured $1/t_\mathrm{p}^2$ spectrum, given as

$$P_t(1/t_\mathrm{p}^2) = \int P_\mathrm{p}(p_\mathrm{p}^2)\Phi(1/t_\mathrm{p}^2, p_\mathrm{p}^2)dp_\mathrm{p}^2\,. \tag{8}$$

where $P_\mathrm{p}(p_\mathrm{p}^2)$ is the sought proton energy distribution, and $\Phi(1/t_\mathrm{p}^2, p_\mathrm{p}^2)$ is the detector $1/\mathrm{TOF}^2$ response function, which describes the averaging over the relevant unobserved quantities. These are θ_0, the angle between proton momentum and magnetic field at the moment of the decay, and the position of the neutron decay. Since the detector $1/\mathrm{TOF}^2$ response function for a given squared proton momentum is narrow, a measurement of $1/t_\mathrm{p}^2$ is approximately equivalent to a measurement of the squared proton momentum p_p^2 (or, the proton energy E_p). The shape of the distribution $P_p(p_\mathrm{p}^2)$ of the proton momentum squared for a given electron energy E_e, reflects the value of a, the neutrino–electron correlation coefficient. The quantity $\cos\theta_{e\nu}$ can be expressed as a function of p_p, the proton momentum, and E_e, the electron energy, which fixes p_e and $p_\nu = (1293\,\mathrm{keV} - E_e)/c$, through

$$p_\mathrm{p}^2 = p_\mathrm{e}^2 + 2p_\mathrm{e}p_\nu\cos\theta_{\mathrm{e}\nu} + p_\nu^2\,, \qquad \text{yielding} \qquad P_p(p_\mathrm{p}^2) = \begin{cases} 1 + a\beta\frac{p_\mathrm{p}^2 - p_\mathrm{e}^2 - p_\nu^2}{2p_\mathrm{e}p_\nu} & \text{for } \left|\frac{p_\mathrm{p}^2 - p_\mathrm{e}^2 - p_\nu^2}{2p_\mathrm{e}p_\nu}\right| < 1\,, \\ 0 & \text{otherwise,} \end{cases} \tag{9}$$

where $\beta = v_\mathrm{e}/c$.

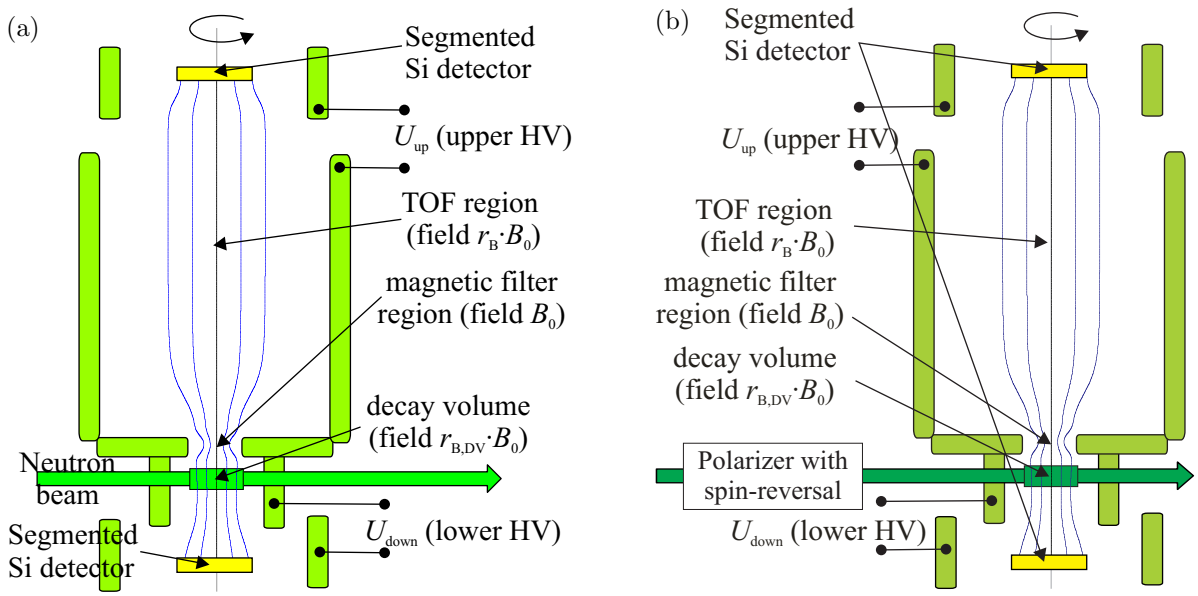

Figure 7: Left sketch, (a): spectrometer setup for the Nab unpolarized neutron decay measurements. Right sketch, (b): in addition to different electric and magnetic field profiles, a polarizer and spin flipper are added to the spectrometer for measurements with a polarized neutron beam. Neither sketch is to scale. The electric and magnetic fields, electrodes (shown in light green), and coils, (not shown), all possess cylindrical symmetry around the vertical axis.

The Si detectors accurately measure the electron energy with keV-level resolution. Electron energy losses through backscattering of electrons are avoided because the magnetic guide field causes every electron to be absorbed in one or the other Si detector, regardless of which detector is impacted first. Corrections for bremsstrahlung and energy losses in the dead layer of the detector have to be made.

The measurement of the proton energy is less accurate because the proton momentum requires a certain minimum distance to be longitudinalized. Compared to the vertical symmetric spectrometer design presented in the original Nab proposal [36], the asymmetric configuration significantly narrows the detector $1/\mathrm{TOF}^2$ response function while maintaining a workable count rate. The width of this function is about 3–4% in the asymmetric configuration, which, through energy smearing, leads to a small but significant correlation between the value of a and its shape. Making the response function narrow decreases the fraction of the proton energy spectrum that is smeared out, and reduces the correlation between the shape of the response function and a. In the original symmetric configuration the neutrons decayed in the region with the maximum magnetic field. The requirements for a large decay volume and a narrow response function were thus in sharp conflict. The optimized asymmetric configuration is shown conceptually in Fig. 7. Beam neutrons decay in a region of moderate magnetic field, and the decay protons have to pass through a field pinch (the filter region) above the decay volume to be detected in the upper detector, the only detector that detects protons. Only upward-going decay protons are accepted in the asymmetric configuration. The lower flight path, not used for the TOF measurement, is relatively short, while the upper flight path, used to measure the proton TOF, is long, leading to a narrow response function. The source height contribution to the width of the resolution function is minimized because the range of accepted proton directions with respect to the magnetic guide field is significantly narrowed by the magnetic field pinch filter.

The overall width of the response function is determined primarily by the sharpness of the magnetic field pinch and the dispersion in the time spent between the decay region and the approach to the field maximum. The time resolution, dominated by the magnetic field properties in the decay and filter regions, is optimized in the present design. This property is further enhanced by an extended low magnetic field region above the filter, which allows for a long average proton time of flight, resulting in a favorable relative width of the response function. Finally, the neutron beam is kept at a higher magnetic field than the detectors, to longitudinalize the electron momenta.

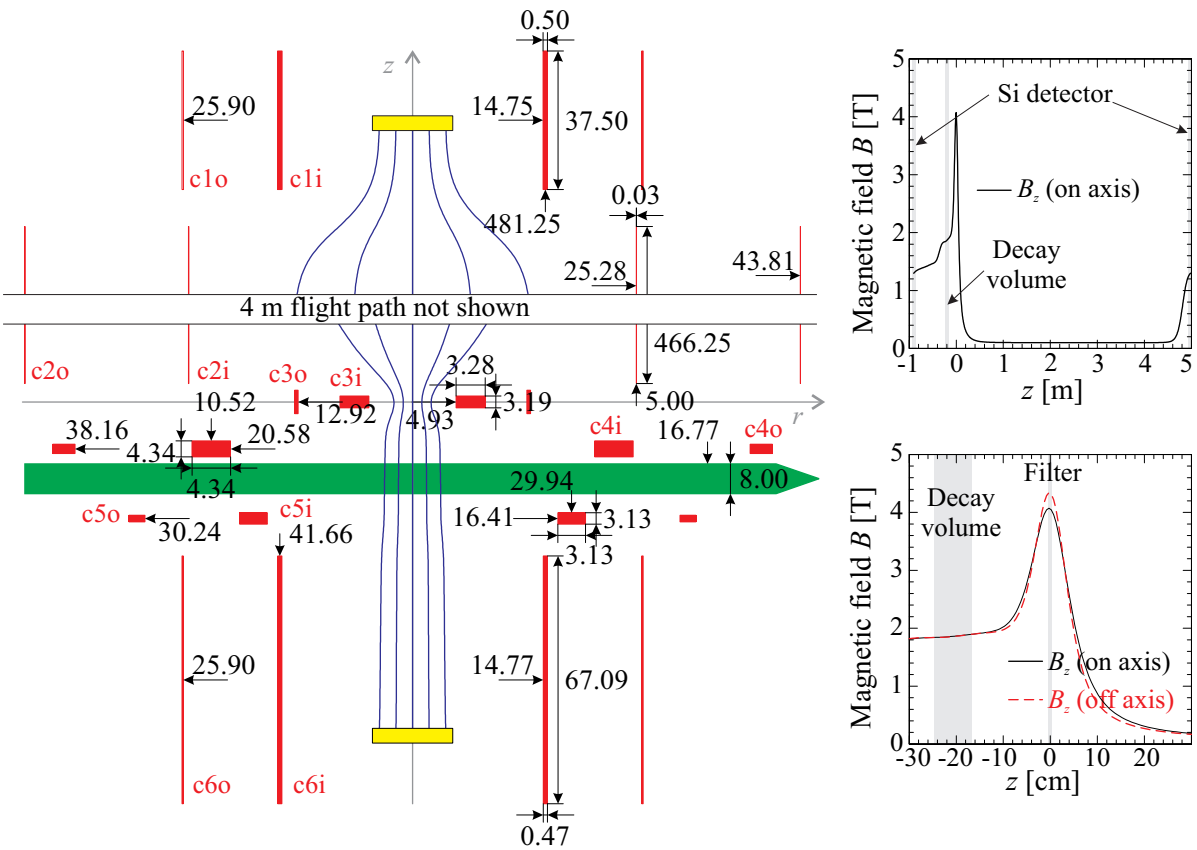

Figure 8: Coil design: The system is cylindrically symmetric around the vertical (z) axis. Vertical distances are given relative to the axis of the coordinate system. All dimensions are given in cm. Coils are drawn in red. The shaded thick green arrow depicts the neutron beam. Magnetic field lines are shown in blue, and the detectors are shown in yellow. About 4 m of space (the drift region) in the center of the coil pair c2i/c2o is omitted in the drawing. The diagrams on the right-hand side depict the magnetic field profiles for the full length of the spectrometer (top), and in more detail for the critical filter region (bottom).

In the adiabatic approximation the upper detector accepts all protons with $\cos\theta_0 \in (\cos\theta_{\min}, 1)$, where $\cos\theta_{\min} = \sqrt{1 - r_{\mathrm{B,DV}}}$, and $r_{\mathrm{B,DV}}$ is the ratio between the magnetic field in decay volume and filter region. A moderate field expansion ratio of $r_{\mathrm{B,DV}} = 0.4$ yields satisfactory event rates for realistic decay volumes.

In the measurement of b, the Fierz interference term, the proposed spectrometer selects only events with protons moving in a limited range of directions. An angular dependence in our detector response function for electrons, e.g., due to electron backscattering, would present the difficult task of disentangling the angular dependence of the electron spectrum of those electrons whose associated protons are detected in the upper detector. However, we have the option to run the spectrometer in a different configuration with the lower detector at $-30\,\mathrm{kV}$, and the remainder of the spectrometer at ground potential (see Fig. 7), plus a mirror voltage of $+1\,\mathrm{kV}$ in the filter region. In this configuration we would detect all protons, and the electron energy distribution is known to be isotropic at the decay point.

A feasible superconducting magnet coil system is shown in Fig. 8. The coil system has cylindrical symmetry around the vertical symmetry axis. The system is actively shielded to comply with the SNS policy about stray magnetic fields: each outer coil has a current orientation opposite to the inner coil. In addition, the entire apparatus will be enclosed in a passive magnetic shield made of steel (not shown in the drawing), similar to the one described in Ref. [41].

The decay volume is a cylinder of radius 3.13 cm, height 8 cm, and volume of $246\,\mathrm{cm}^3$. The expected neutron decay rate is about $2{,}500\,\mathrm{s}^{-1}$, out of which 13% of the protons are detected in the upper detector.

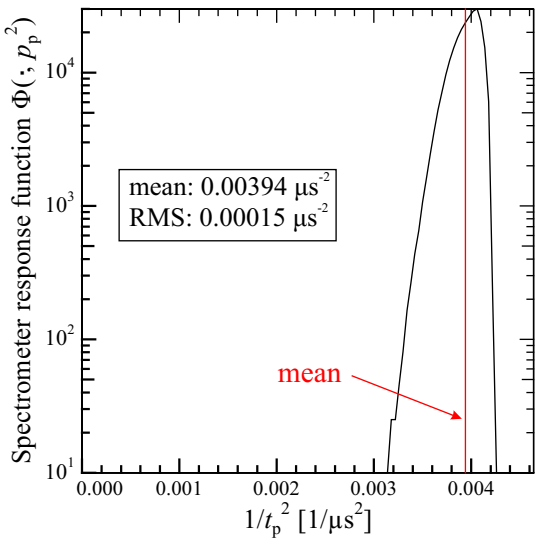

Figure 9: Detector $1/\mathrm{TOF}^2$ response function: Detector response for a proton with momentum $p_p^2 = 0.95\,\mathrm{MeV/c}$.

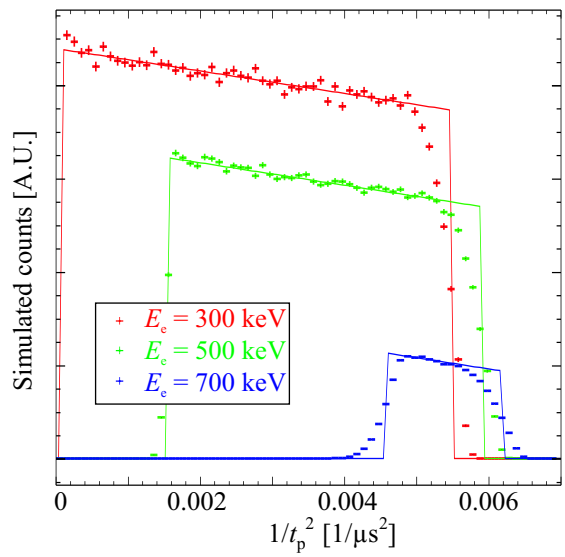

Figure 10: Proton $1/t_\mathrm{p}^2$ spectrum for different values of fixed electron energy E_e. The solid line is the expectation for an infinitely sharp detector $1/\mathrm{TOF}^2$ response function.

GEANT4 simulations have demonstrated that the detector $1/\mathrm{TOF}^2$ response function in this configuration has a relative width (defined as RMS/mean) of 3.8% (Fig. 9). The simulation whose results are depicted in Fig. 9 neglects small corrections due to the acceleration field, and the electron TOF.

Figure 10 shows the proton $1/t_\mathrm{p}^2$ spectrum for different electron energies E_e. The data points are the results of a GEANT4 simulation. The solid lines show the expectation for a detector $1/\mathrm{TOF}^2$ response function which is infinitely sharp. For a perfect detector, the $1/t_\mathrm{p}^2$ spectrum would have a slope proportional to a, the neutrino–electron correlation coefficient, within the range of $1/t_\mathrm{p}^2$ allowed by the decay kinematics, and would drop sharply to zero outside (see Eqs. (8) and (9) and the original Nab proposal [36]). The main effect of the realistic detector $1/\mathrm{TOF}^2$ response function is to soften these edges. The measured data at the edges can be used to determine the detector $1/\mathrm{TOF}^2$ response function experimentally.

We next turn to the relationship between t_p, the proton TOF, and p_p, the proton momentum, in order to determine $\Phi(1/t_\mathrm{p}^2, p_\mathrm{p}^2)$, the detector $1/\mathrm{TOF}^2$ response function. In the adiabatic approximation t_p is given by [36, 42]:

$$t_\mathrm{p} = \frac{m_\mathrm{p}}{p_\mathrm{p}} \int \frac{dz}{\sqrt{1 - \frac{B(z)}{B_0}\sin^2\theta_0 - \frac{e(U(z)-U_0)}{T_0}}}\,, \tag{10}$$

where m_p is the proton mass, while B_0 and U_0 are the magnetic field and electric potential, respectively, at the point of decay. The initial values are taken for p_p and T_0, the proton momentum and energy, respectively. The proton gyrates around a magnetic field line, and the integral is taken along this field line from its initial value at the decay point all the way to the detector. Imperfect knowledge of the detector $1/\mathrm{TOF}^2$ response function is the principal source of systematic uncertainties. The main contribution to the width of $\Phi(1/t_\mathrm{p}^2, p_\mathrm{p}^2)$ in Fig. 9 comes from the different times of flight to the detector for protons with equal energy but different emission angle θ_0 relative to the magnetic field. The most important property of the spectrometer influencing the spread in the proton TOF for a given p_p is the magnetic field in the filter region. Our optimization resulted in a compromise between a very high field curvature in the filter region (i.e., a narrow detector $1/\mathrm{TOF}^2$ response function), and a reasonably big decay volume (i.e., a coil c3i that is not too small).

Finally, detector choice and design have presented a challenge. The detector has to be able to stop and detect the full energy of 50–750 keV electrons as well as 30 keV protons. This requires a detector thickness of about 2 mm Si-equivalent, a very thin window technology, and a very low energy threshold for detecting

signals down to about 10 keV.

The very thin window, or dead layer, should uniformly cover a large area of $\simeq$100 cm^2. The detector has to be segmented into about 100 elements. The segmentation has to be applied on the back side to keep the irradiated front side homogeneous. The segmentation is necessary to determine the particle position and thus to identify the electron or proton trajectory. The time and spatial pattern of electron energy deposition has to be measured. The detector segmentation has to be combined with pulse processing electronics allowing for real-time signal recording with a resolution at the level of several ns. The low energy threshold is related to good energy resolution, at the level of a few keV for the relevant energy range of electrons and protons.

A cooled silicon detector has the optimal combination of efficiency, stability, energy resolution and timing resolution unsurpassed by other types of detector, some of which may excel in one of the above characteristics, but not in all. The design goal, pursued in a collaboration with Micron Semiconductor Ltd., has been to build a large area segmented single wafer silicon detector, about 2 mm thick to enable stopping the electrons, and operating with liquid nitrogen cooling at the temperature level of about 100 K. Charged particles enter the detector through the junction side, which is uniform, apart from a very thin aluminum grid deposited on it with a coverage of 0.4%. Charge liberated by the ionizing particles is collected on the ohmic side. A photograph of a sample, fully operational prototype detector is shown in Fig. 11.

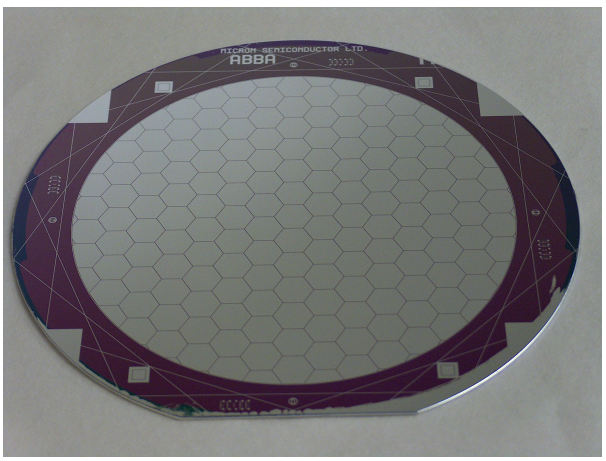

Figure 11: Photograph of a prototype full-size Si detector developed for abBA and Nab experiments. Depicted is the ohmic, readout side of the detector. The 127 hexagons, with side length $s_d = 5.2$ mm and area $A_d = 70$ mm^2, represent individual detector elements, each read out separately. Hexagons fill the circular area of the detector efficiently, and they match the image of the decay volume well. Only three detector elements meet at a single vertex, thus reducing the maximum number of elements involved in a charge-sharing event. Although the detector is segmented, there are no dead spaces between the detector elements.

Micron Semiconductor have constructed prototype detectors that satisfy all of the design criteria. Prototype detectors have been throughly tested with alphas and photons, with excellent results. As of this writing, only tests with 30 keV protons remain to be done (they have been delayed primarily due to the limited beam availability on an appropriate source), but are planned to be performed in the near future.

Designs of a load-lock mechanism, necessary at each end of the magnet to remove the detectors for servicing, have been completed. The design and implementation of the detector enclosure, mounting structure, readout and cooling, are complicated by the requirement that the detectors be operable at 30 keV with respect to ground.

2.3. Measurement of polarized neutron decays

The asymmetric Nab spectrometer, as shown in Fig. 7, will be used for subsequent polarized neutron decay measurements, abBA and PANDA. The basic setup for the polarized runs is shown in Fig. 7(b). For a measurement of the electron asymmetry we plan to use a configuration like the one for b, the Fierz Interference term discussed earlier, with the electrostatic voltages set in such a way that all protons are detected in the lower detector. The coincidence between electrons and protons from the same neutron decay, one of the main features of abBA that strongly suppresses of background uncertainty, is preserved. A proton asymmetry is measured with the upper detector serving as the proton detector, as in the measurement of a, the neutrino electron correlation. A measurement of the asymmetry in the proton count rate with respect to the proton spin as a function of the electron energy can be transformed into a measurement of B, as shown in Ref. [21].

As already noted, the most recent published versions of the abBA and PANDA proposals [45, 46] are

based on an earlier design with symmetric flight paths towards the two detectors. The abBA proposal argues that a statistical uncertainty of $\Delta A/A = 0.14\%$ and $\Delta B/B = 0.08\%$ can be achieved in such a setup. Important contribution to the systematic uncertainty were the knowledge of the degree of the neutron beam polarization $P_{\rm n}$, and the magnetic mirror effect. The proposal argues that $\Delta P_{\rm n}/P_{\rm n} = 5 \times 10^{-4}$ is within reach, equal to the uncertainty in the most recent PERKEO II run [14].

The neutron beam polarization is independent of the spectrometer design, as are most of the other contributions to the systematic uncertainty. Here we discuss the contributions to the systematic uncertainty which are substantially different for an abBA is performed in the common asymmetric spectrometer, as proposed here:

1. **Statistical uncertainty:** We anticipate a count rate considerably higher than 40 Hz, the count rate used in Ref. [45], which was the basis for the predicted estimate of the statistical uncertainty of $\Delta A/A \sim 10^{-3}$ and $\Delta B/B \sim 10^{-4}$. The bigger decay volume and the higher sensitivity of the asymmetric spectrometer due to the magnetic filter that lets through for detection only the electrons with the highest value of asymmetry, outweigh the reduction in solid angle due to the magnetic filter. The enhancement of the statistical sensitivity due to a restriction of the accepted solid angle is discussed at length in Ref. [47].

2. **Solid angle:** The asymmetric spectrometer design replaces the unwanted magnetic mirror effect, source of the highest contribution to the expected systematic uncertainty in the original abBA [45], is replaced by the requirement to determine the solid angle of the upper detector. We have shown in a recent update [38] that we can combine the measured electron asymmetries in upper and lower detectors in such a way that the solid angle drops out. We can also combine the measured electron asymmetry in a different way that allows us to extract the solid angle of the upper detector *in situ*, e.g., for subsequent use in a proton asymmetry measurement. Furthermore, we have shown that the magnetic field inhomogeneity in the decay volume can be neglected in this procedure. Therefore, no high precision magnetic field measurements are needed, and the systematic uncertainty due to the solid angle of the detector drops out.

   We note that the usual arrangement with two identical detectors used for electron and proton asymmetry measurements, is replaced by two different detectors, but with a difference which is precisely understood.

3. **Particle trapping:** The asymmetric spectrometer design completely avoids problems due to particle trapping and Penning discharges in the originally proposed abBA symmetric apparatus [45], where two detectors, connected by magnetic field lines, are both set at -30 kV with respect to the volume in between.

4. **Electric field homogeneity:** The proton asymmetry is highly sensitive to electric potential inhomogeneities. In the configurations discussed in Refs. [45] and [46], having the decay volume in an (unwanted) electrostatic potential trap only 1 mV deep, increases the measured proton asymmetry by 0.17% (the error increases with the square root of the trap depth). Previous work has showed that it is very hard to reduce work function inhomogeneities, or surface charges, to this level (see, e.g., Refs. [48, 49, 50]). An unwanted potential gradient is equally bad, but its effect cancels to first order if the average of the measured asymmetry between upper and lower detector is evaluated. It is possible to reduce the sensitivity to an electrostatic potential trap if the analysis is restricted to certain proton or electron energies, eliminating the pernicious low energy protons.

   The sensitivity to electric potential traps is practically in a proton asymmetry measurement using the common spectrometer discussed in this proposal. The leading contribution is an (unwanted) electric potential difference between the filter region and the decay volume. A filter–decy potential difference as large as 500 mV changes the proton asymmetry by less than 0.04% (for $r_{\rm B,DV} = 0.5$).

In summary, the asymmetric common spectrometer design removes significant problem points of the original symmetric abBA design, and improves the systematic uncertainties, while preserving the high statistical sensitivity.

Table 1: Statistical uncertainty in the determination of a in Method B, and the influence of different cuts.

lower E_e cutoff:	none	100 keV	100 keV	300 keV
upper t_p cutoff:	none	none	100 μs	40 μs
σ_a	$2.4/\sqrt{N}$	$2.5/\sqrt{N}$	$2.5/\sqrt{N}$	$2.5/\sqrt{N}$
σ_a (E_{cal}, l variable)	$2.5/\sqrt{N}$	$2.6/\sqrt{N}$	$2.6/\sqrt{N}$	$2.7/\sqrt{N}$
σ_a (inner 70% of data)	$4.1/\sqrt{N}$	$4.1/\sqrt{N}$	$4.1/\sqrt{N}$	$4.1/\sqrt{N}$

2.4. Dominant uncertainties in the determination of *"a"*

The neutrino–electron correlation coefficient a is determined in a χ^2-fit to the two dimensional function P_t, introduced in Eq. (8), which depends on t_p, proton TOF, and on E_e, electron energy. The fitting parameters are: a, N, the number of decays, b, the Fierz interference term, and eventually additional parameters which characterize spectrometer properties.

Our plan is to analyze the data, to the best extent possible, first with method B, introduced and extensively discussed in Refs. [36, 38]. In this method, our knowledge of the spectrometer properties, as determined from auxiliary measurements, is converted into a prediction of the shape of $\Phi(1/t_p^2, p_p^2)$. We perform the fit twice. First, we use the full data set and two additional fit parameters, the average value of the detector $1/\mathrm{TOF}^2$ response function (parametrized as length of flight path L), and an electron energy calibration factor (E_{cal}). In a second step, we fix the additional parameters, and reduce our data set by taking only the inner 70% of the data in the $P_t(1/t_p^2)$ distribution for each given electron energy E_e. This procedure makes use of the fact that the edges of $P_t(1/t_p^2)$ distribution are mainly sensitive to the shape of the detector $1/\mathrm{TOF}^2$ response function $\Phi(1/t_p^2, p_p^2)$, and the inner part is mainly sensitive to the neutrino electron correlation coefficient a. The decision to use only the inner 70% of the data sample in the second fit reduces the statistical sensitivity by 65%, which is offset by considerably relaxed tolerances for a number of false effects (sources of systematic uncertainty).

The statistical uncertainty is shown in Table 1 for several possible threshold values for the electron energy ($E_{e,min}$), and $t_{p,max}$, a high proton TOF cutoff due to accidental coincidences. N is the number of decays in which the proton goes into the upper detector, irrespective of further cuts.

Omission of b, i.e., setting $b \equiv 0$ for a fit within the standard model, would not improve the uncertainty in a. A total of 1.6×10^9 events are required to determine a with a relative statistical uncertainty of 10^{-3}. About 8 weeks of live data taking are needed for a single run, without extra measurements devoted to systematic checks.

The most important associated systematic uncertainties are discussed in detail in the Nab proposal update [38]. We present in Table 2 only a summary of the uncertainties in the determination of a. Some sources of uncertainty are marked with an asterisk. These parameters can be determined from the edges of the $P_t(1/t_p^2)$ distribution in the primary data, so a separate dedicated measurement is not necessary.

Analysis Method A, discussed in Refs. [36] and[38], will go beyond what can be achieved with Method B. We will reconstruct the detector $1/\mathrm{TOF}^2$ response function in greater detail from the shape of the measured $P_t(1/t_p^2)$ distribution. This approach introduces more free parameters. We rely on Method B to provide good starting values for the parameters; otherwise the fitting procedure used to determine the optimum values for the free parameters may not be numerically stable. The choice of the parameters and their functional relationship to the detector response function are discussed in Ref. [38]. A successful application of Method A would lead to a substantial reduction of the systematic uncertainties reported in Table 2.

2.5. Principal uncertainties in the determination of *"b"*

Careful attention to understanding details of the spectrometer response to both protons and electrons discussed above also helps to reduce the systematic uncertainties in the measurement of b. Measuring b amounts to a precise determination of the shape of the electron spectrum and its deviation from the $b = 0$ shape predicted by the standard model. Any such deviation will be far more pronounced at low electron momenta than for high momenta. Therefore the accurate understanding of background rates, which increase

Table 2: Systematic uncertainties in the determination of a due to imperfect knowledge of spectrometer properties in Method B. Parameters marked with asterisks can be determined from the edges of the $P_t(1/t_{\rm p}^2)$-distribution in the primary data, so a separate dedicated measurement is not necessary. The uncertainties are added in quadrature to obtain the total.

Experimental parameter	Systematic uncertainty $\Delta a/a$
Magnetic field	
... curvature at pinch	5×10^{-4}
... ratio $r_{\rm B} = B_{\rm TOF}/B_0$	2.5×10^{-4}
... ratio $r_{\rm B,DV} = B_{\rm DV}/B_0$	3×10^{-4}
Length of the TOF region	(*)
Electrical potential inhomogeneity:	
... in decay volume / filter region	5×10^{-4}
... in TOF region	1×10^{-4}
Neutron Beam:	
... position	4×10^{-4}
... width	2.5×10^{-4}
... Doppler effect	small
Adiabaticity of proton motion	1×10^{-4}
Detector effects:	
... Electron energy calibration	(*)
... Electron energy resolution	5×10^{-4}
... Proton trigger efficiency	2.5×10^{-4}
Residual gas	small
Background	small
Sum	1×10^{-3}

with decreasing pulse size, is crucial. The coincidence method will help us to reduce the background rates. Momentum dependence of electron detection efficiency, especially near threshold, and electron spectrum distortions due to reflections at the detector surface and elsewhere in the spectrometer, must be controlled. The calibration methods outlined above generally bring us to the desired level. We have initiated work on a realistic Monte Carlo simulation of the background. Such simulations can only be taken as a guideline; eventually the backgrounds will have to be measured and dealt with *in situ* because of the complexity of the apparatus.

The statistical uncertainty in b is given in Table 3, which is in agreement with the calculations of Ref. [21]. Here, again, N is the number of neutron decays. N is not restricted to the subset in which electrons and protons pass the respective cutoff conditions. The statistical uncertainty of b increases quickly if a high electron energy threshold is chosen. The reason is that at higher electron energies a non-zero value of b looks similar to a change of the normalization N. Therefore, the fitting parameters N and b are strongly correlated.

Table 3: Statistical uncertainty in the determination of the Fierz Interference term b, and the influence of an electron energy cut.

lower $E_{\rm e}$ cutoff:	none	100 keV	200 keV	300 keV
σ_b	$7.5/\sqrt{N}$	$10.1/\sqrt{N}$	$15.6/\sqrt{N}$	$26.4/\sqrt{N}$
σ_b ($E_{\rm cal}$ variable)	$7.7/\sqrt{N}$	$10.3/\sqrt{N}$	$16.3/\sqrt{N}$	$27.7/\sqrt{N}$

The second line of Table 3 lists the statistical uncertainty in b if the energy calibration is determined from a fit to the beta spectrum. The statistical uncertainty is not significantly worse than that obtained

with a fixed energy calibration.

For an overall sample of 5×10^9 decays, the statistical uncertainties σ_b calculated on the basis of the above table are in the range of $\sigma_b \sim 10^{-4}$, far better than our goal of overall uncertainty of $\sim 10^{-3}$. It is clear that the main challenge in the measurement of b will be in the systematics. While we have indicated strategies for controlling the systematics, a major contribution will be the electron background, which will ultimately have to be evaluated, and dealt with, *in situ*.

2.6. Instrument development and project resources

This MRI proposal to the NSF is accompanied by a funding request to the DOE for the remaining subsystems of the Nab/abBA apparatus not included here. These items include the neutron beamline, radiological shielding, Si detectors, and data acquisition (DAQ) system. The relevant DOE office has communicated its intention to fund their part of the program provided the NSF MRI is approved.

This development MRI proposal goes well beyond the mere acquisition of a superconducting magnet system. For one, the custom magneto-electrostatic apparatus is being designed and optimized by the collaboration under the leadership of the UVa group, and is far different from any standard device. Critical design activities will continue throughout the ordering and construction phases, in close collaboration with the engineers of the cryo-magnet supplier and ORNL. In addition to being optimized for, and fully meeting the requirements of the Nab and abBA experiments, the spectrometer magnet also requires the passive magnetic shield, as well as the HV electrode and vacuum systems, all of which are essential parts of the present MRI request. The primary design as well as the responsibility for ensuring that all of these systems are compatible, for their assembly into a complete apparatus, for the testing of individual components, as well as for the testing of the apparatus as a whole, rests on the collaboration members, specifically members of this consortium. Thus the development, procurement and testing phases will involve the university groups and the eventual vendors in a collaborative effort.

The partners in this MRI development consortium are UVa, ASU and ORNL. The UVa group has the leading role in the MRI project. It has originated the conceptual, as well as the detailed design, and will continue to work on further design development with vendors of all systems: cryo-magnet, electrostatic electrodes, HV, and vacuum to ensure compatibility and full functionality. The ASU group has the responsibility for the passive magnetic shield, and will continue to collaborate on its design and development. ORNL will host the instrument, provide the necessary space, engineering and technical support to integrate it into the laboratory, and will help with the instrument's maintenance during the measurement years in a manner that enables its full-scale operation.

Nab, and the abBA experiment after it, will be carried out by broad international collaborations. At his time the collaborations include some 30 members from 15 institutions, with a large overlap between them. The various groups have clearly identified responsibilities in the projects. Besides groups from USA, Canada and Europe, we also have collaborators from Mexico.

Even though the Nab and abBA experiments are far from taking data, they have already involved a number of students in various design and development tasks. Multiple graduate students from UVa, ASU, North Carolina State University, and other groups, have been active on aspects of design, development and prototype testing of various components of the apparatus. Since many of the low-level subprojects have a clearly defined scope and duration, they lend themselves very well to undergraduate student participation. At UVa alone, four undergraduate students have been involved to date, one of whom, Rachel Hodges, won the Physics department's Undergraduate Research Prize in 2009.

2.7. Scheduling and budget considerations

Table 4 summarizes the significant milestones in the project timetable of this MRI, while Table 5 lists other related significant milestones up to the completion of Nab data taking. The tables present an optimal scenario which does not assume major technical, administrative or funding delays. The budget items associated with milestones in Table 4 are discussed in detail in the Budget Justification accompanying this proposal.

Table 5 shows the time schedule for other, largely parallel, subprojects needed to prepare for the initial use of the spectrometer in the Nab configuration, i.e., with unpolarized neutrons. The critical path in the preparatory stages of the Nab project schedule is dominated by the design, procurement, and successful testing of the magneto-electrostatic spectrometer.

Table 4: Table of significant milestones in the schedule of the development of the magneto-electrostatic spectrometer for the study of neutron beta decay.

	Milestone	Completion
	Start of project	July 2011
0.	**Magnet design ready for bidding**	**Sep. 2011**
1.a	Order for magnet placed (design & option to build)	Jan. 2012
1.b	Acceptance of engineering drawings	Dec. 2012
1.c	Delivery of magnet	Sep. 2013
1.	**Spectrometer magnet accepted**	**Dec. 2013**
2.a	Magnetic shielding calculation for Nab approved	Sep. 2012
2.b	Permissions in place to allow installation of Magnetic Shield	Jun. 2013
2.b	All necessary parts procured, machined, and at ORNL	Sep. 2013
2.	**Passive Magnetic Shield ready**	**Dec. 2013**
3.a	Electrode material selection	Mar. 2013
3.b	Electrode system assembled	Mar. 2014
3.	**Electrode system ready**	**Dec. 2013**
4.a	HV in main vacuum system demonstrated	Sep. 2013
4.b	UHV in main and detector vacuum systems demonstrated	Dec. 2013
4.	**Vacuum system ready**	**Mar. 2014**

Table 5: Table of other milestones in the time schedule up to the completion of the Nab experiment.

	Milestone	Date
5.a	Modification of radiological shielding at FNPB ready	Dec. 2013
5.b	Modification of utilities at FNPB ready	Jan. 2014
5.	**FNPB beamline modifications ready**	**April 2014**
6.a	Detector shielding available	Feb. 2014
6.b	Beam control and characterization equipment available	May 2014
6.	**Detector shielding and beam control ready**	**Aug. 2014**
7.a	Neutron guide calculations for incoming neutron beam accepted	Sep. 2013
7.b	Incoming neutron beam line installed	Jun. 2014
7.	**Neutron beam line ready**	**Sep. 2014**
8.a	Detector test stand available	Mar. 2012
8.b	First detectors characterized (test stand, proton source)	Sep. 2013
8.c	Detector mechanics ready	Dec. 2013
8.	**Detectors ready**	**Jun. 2014**
9.a	DAQ electronics and Trigger working	Sep. 2013
9.b	Data storage and slow control ready	Mar. 2014
9.	**DAQ system ready**	**June 2014**
10.a	Magnetometer calibrated	Sep. 2012
10.b	Magnetic field mapping system constructed	Dec. 2013
10.	**Magnetic field of spectrometer mapped**	**Mar. 2014**
	Start of data taking for Nab	**Oct. 2014**
	Switchover to abBA configuration	**Oct. 2015**

References

1. Review of Particle Physics, J. Phys. G **37**, 1 (2010), updated online at `http://pdg.lbl.gov/`.
2. F.J. Gilman, K. Kleinknecht and B. Renk, in *"Review of Particle Physics"*, K. Hagiwara et al., Phys. Rev. D **66**, 01001-113 (2002).
3. A. Sher et al. (BNL 865 Collaboration), Phys. Rev. Lett. **91**, 261802 (2003).
4. T. Alexopoulos et al. (KTeV Collaboration), Phys. Rev. Lett. **93**, 181802 (2004).
5. A. Lai et al. (CERN NA48 Collaboration), Phys. Lett. B **602**, 41 (2004).
6. W.J. Marciano, A. Sirlin, Phys. Rev. Lett. **96**, 032002 (2006).
7. J. Hardy, I. Towner, Phys. Rev. C **79**, 055502 (2009).
8. G.A. Miller and A. Schwenk, Phys. Rev. C **78**, 035501 (2008).
9. G.A. Miller and A. Schwenk, arXiv 0910.2790 (2009).
10. N. Auerbach, Phys. Rev. C **79**, 035502 (2009).
11. H. Liang, N. Van Giai, and J. Meng, Phys. Rev. C **79**, 064316 (2009).
12. I. Towner, J. Hardy, Phys. Rev. C **82**, 065501 (2010)
13. J. Liu et al.(UCNA collaboration), Phys. Rev. Lett. **105**, 181803 (2010).
14. H. Abele, private communication (2009).
15. H. Abele et al., Phys. Rev. Lett. **88**, 211801 (2002).
16. P. Liaud et al., Nucl. Phys. A **612**, 53 (1997).
17. B. Yerozolimsky et al., Phys. Lett. B **412**, 240 (1997).
18. P. Bopp et al., Phys. Rev. Lett. **56**, 919 (1986).
19. Yu. Mostovoĭ et al., Phys. At. Nucl. **64**, 1955 (2001).
20. O. Naviliat-Čunčić and N. Severijns, Phys. Rev. Lett. **102**, 142302 (2009).
21. F. Glück et al., Nucl. Phys. A **593**, 125 (1995).
22. T.D. Lee, C.N. Yang, Phys. Rev. **104**, 254 (1956).
23. J.D. Jackson, S.B. Treiman, H.W. Wyld, Phys. Rev. **106**, 517 (1957).
24. G. Konrad, W. Heil, S. Baeß ler, D. Počanić, F. Glück Proceedings of the 5th International BEYOND 2010 Conference, Cape Town, South Africa (2010), World Scientific (arXiv 1007.3027)
25. A. Serebrov et al., Phys. Lett. B **605**, 72 (2005).
26. A. Pichlmaier et al., Phys. Lett. B **693**, 221 (2010).
27. N. Severijns, M. Beck, O. Naviliat-Čunčić, Rev. Mod. Phys. **78**, 991 (2006).
28. C.A. Gagliardi, R.E. Tribble, and N.J. Williams, Phys. Rev. D **72**, 073002 (2005).
29. S. Profumo, M.J. Ramsey-Musolf and S. Tulin, Phys. Rev. D **75**, 075017 (2007).
30. V. Cirigliano, private communication (2009).
31. M. Bychkov, et al., Phys. Rev. Lett. **103**, 051802 (2009).
32. P. Herczeg, private communications (2004) and (2010).
33. `http://pibeta.phys.virginia.edu/`.
34. `http://pen.phys.virginia.edu/`.
35. `http://pienu.triumf.ca/`.
36. R. Alarcon et al., Nab experiment proposal, 2007, `http://nab.phys.virginia.edu/nab_proposal.pdf`.
37. D. Počanić et al., Nucl. Inst. Meth. A **611**, 211 (2009).
38. R. Alarcon et al., Nab proposal update, Jan 2010, `http://nab.phys.virginia.edu/nab_doe_fund_prop.pdf`.

39. P. Huffman et al., Beamline Performance Simulations for the FnPB, private communication, 2005. Initial measurements performed in the FnPB up to the time of this writing are in excellent agreement with the simulation.
40. J. Byrne et al., J. Phys. G: Nucl. Part. Phys. **28**, 1325 (2002).
41. G. Konrad et al., Proceedings of the European COMSOL conference, Grenoble, 2007, `http://cds.comsol.com/access/dl/papers/3276/Konrad.pdf`.
42. F. Glück et al., Eur. Phys. J. A **23**, 135 (2005).
43. B. Hubbard-Nelson et al., Nucl. Inst. Meth. A **422**, 411 (1999) and `http://www.xia.com`.
44. R. Grzywacz et al., Nucl. Inst. Meth. B **204**, 649 (2003).
45. R. Alarcon et al., abBA-Proposal, 2007, `http://nab.phys.virginia.edu/ABBA_proposal_2007.pdf`.
46. R. Alarcon et al., PANDA - Precision Measurement of the Proton Asymmetry in Neutron Decay, Sep 2008, `http://research.physics.lsa.umich.edu/chupp/PANDA/PANDA\spacefactor\@mSNS.pdf`.
47. D. Dubbers et al., Nucl. Inst. Meth. **596**, 238 (2008).
48. R. Dobrozemsky, Nucl. Inst. Meth. **118**, 1 (1974).
49. N. A. Robertson et al., Class. Quant. Grav. **23**, 2665 (2006).
50. S. Baeßler et al., Eur. Phys. J. A **38**, 17 (2008).
51. D. Dubbers et al., arXiv:0812.0347.
52. S.G. Tagare, Phys. Rev. A **34** 1587 (1986).
53. M. Simson et al., Nucl. Inst. Meth. A**611**, 203 (2009).
54. M.A. Lone et al., Nucl. Inst. Meth **174**, 521 (1980).
55. J.S. Nico et al., Phys. Rev. C **71**, 055502 (2005).
56. F. Glück, Phys. Lett. B **436**, 25 (1998).